Interplay between Kelvin-Helmholtz and current-driven instabilities in jets

H. Baty

Observatoire Astronomique, 11 Rue de l'Université, 67000 Strasbourg, France.

baty@astro.u-strasbg.fr

and

R. Keppens

FOM-Institute for Plasma Physics Rijnhuizen,
P.O. Box 1207, 3430 BE Nieuwegein, The Netherlands.

keppens@rijnh.nl

ABSTRACT

We investigate, by means of three dimensional compressible magnetohydrodynamic numerical simulations, the interaction of Kelvin-Helmholtz (KH) and current-driven (CD) instabilities in a magnetized cylindrical jet configuration. The jet has a supersonic axial flow, sheared in the radial direction, and is embedded in an helical magnetic field. The strength of the axial magnetic field component is chosen to be weak, in accord with the 'weak field regime' previously defined by Ryu, Jones & Frank for uniformly magnetized configurations. We follow the time evolution of a periodic section where the jet surface is perturbed at $m = \pm 1$ azimuthal mode numbers. A $m = -1$ KH surface mode linearly develops dominating the $m = +1$ KH one, in agreement with results obtained using an independent ideal stability code. This lifted degeneracy, due to the presence of the helical field, leads nonlinearly to clear morphological differences in the jet deformation as compared to uniformly magnetized configurations. As predicted by stability results, a $m = -1$ CD instability also develops linearly inside the jet core for configurations having a small enough magnetic pitch length. As time proceeds, this magnetic mode interacts with the KH vortical structures and significantly affects the further nonlinear evolution. The magnetic field deformation induced by the CD instability provides a stabilizing effect through its azimuthal component B_θ. This helps to saturate the KH vortices in the vicinity of the jet surface. Beyond saturation, the subsequent disruptive effect on the flow is weaker than in cases having similar uniform and helical magnetic field configurations without CD mode. We discuss the implications of this stabilizing mechanism for the stability of astrophysical jets.

Subject headings: Instabilities– MHD – methods : numerical – plasmas

1. Motivation

The Kelvin-Helmholtz (KH) instability plays a crucial role in numerous astrophysical plasmas where sheared flows are present. This is certainly the case in collimated jets from active galactic nuclei (AGN) and young stellar objects (Birkinshaw 1991; Ferrari 1998). High resolution hydrodynamic simulations of supersonic jets have shown how the development of KH modes can nonlinearly lead to the formation of shocks, entrainment and mixing with the ambient material, and ultimately to disruption on a few sound transit time scales (Bodo et al. 1995, 1998). In terms of the azimuthal mode number m, the $m = \pm 1$ surface modes, which involve large-scale helical distortions of the interface separating the jet from the ambient medium, appear to be the most dangerous ones for the integrity of the flows. It is then very difficult to explain the remarkable stability and coherence of observed astrophysical jets over long distances in comparison with their radial extents.

Generally, collimated astrophysical jets are magnetized. Most of the literature on magnetohydrodynamic (MHD) jet stability has focused on subsonic flows embedded in uniform magnetic fields. Depending on the Alfvén Mach number $M_{A,z} = V/v_{A,z}$ of the background configuration, where V is the shear flow amplitude and $v_{A,z}$ is the Alfvén speed projected along the flow direction, four regimes characterizing the development of KH surface instabilities in cartesian geometry have been identified, both in two dimensional studies (Malagoli, Bodo, & Rosner 1996; Frank et al. 1996; Jones et al. 1997, Keppens et al. 1999), as well as more recently in three dimensional (3D) simulations (Ryu, Jones, & Frank 2000). The flow is *linearly stable* if the magnetic tension of the initial magnetic field component parallel to the flow is so strong as to prevent the development of a small perturbation of the shear layer. This first regime holds for $M_{A,z} \lesssim 2$. When $4 \gtrsim M_{A,z} \gtrsim 2$, the initial magnetic field can not provide linear stability, but the flow can be nonlinearly stabilized by the magnetic tension generated by the perturbed shear layer. This second regime is referred to as the *strong field* or the *nonlinearly stable* regime. In a weaker magnetic field configuration, the shear layer can roll-up while vortices are forming. Meanwhile, the magnetic field lines are stretched, twisted, and amplified around the vortices perimeter. A nonlinear saturation then occurs by the end of a single vortex rotation, when the magnetic field becomes locally dominant. This saturation stage has been described in detail using 3D cylindrical jet simulations (Keppens and Tóth 1999). The saturated patterns prominently feature 3D sheet-like and tubular fibril structures that are the generalization of the Kelvin's cat's eyes obtained in 2D MHD studies. Alternating regions of density enhancement and depletion coincide with regions of low and high magnetic field strength, respectively. As this evolution also leads to magnetic reversals, the cat's eye structure is subsequently rapidly broken up due to magnetic reconnection. This *weak field* regime is therefore qualified as *disruptive*, and occurs for $50 \gtrsim M_{A,z} \gtrsim 4$. Finally, another regime is obtained when $M_{A,z} \gtrsim 50$. The development of KH instabilities in this *very weak field* regime is essentially hydrodynamic in early stages, but eventually triggers decaying MHD turbulence accompanied by magnetic reconnection events (Ryu et al. 2000). Out of these four physically distinguishable regimes, one may argue that weak fields in the disruptive regime are of crucial importance in modifying substantially the nonlinear evolution of KH instabilities – compared to a pure hydrodynamic case. Therefore, this regime may play a role in maintaining a large-scale coherent flow.

However, uniformly magnetized jet simulations inadequately represent magnetized astrophysical jets possessing an helical field configuration. In such jets, the magnetic tension due to the azimuthal field component can provide an effective collimation mechanism (see discussion in Sect. 2 of Appl & Camenzind 1992). Such helical magnetic configurations have a non zero electric current density. An ideal stability study has shown that current-carrying jets have KH modes which are slightly stabilized when compared to configurations having a uniform longitudinal magnetic field with the same fast magnetosonic Mach number (Appl and Camenzind 1992). On the other hand, such jets are also liable to other, pure MHD instabilities driven by the current density parallel to the magnetic field and by the thermal pressure gradient. The latter, pressure-driven instabilities are radially localized modes characterized by high wavenumbers and are likely responsible for generating MHD turbulence in the jet core (Begelman 1998; Kersalé, Longaretti, & Pelletier 2000). The former current-driven (CD) instabilities are internal modes growing in the jet frame in a fraction of the radial Alfvén crossing time, when the pitch length of the field lines is small compared to the jet radius (Appl, Lery & Baty 2000). Dominant CD instabilities are global modes having $m = \pm 1$ azimuthal mode numbers, which mainly lead to a nonlinear redistribution of the current density within the jet core (Lery, Baty, & Appl 2000).

The aim of the present paper is to investigate how the presence of CD modes affects the nonlinear evolution of KH surface instabilities. A jet flow directed along the axial direction and sheared in the radial one is considered. The sonic and fast magnetosonic Mach numbers are taken to be 1.26 and 1.24 on jet axis, respectively. These slightly supersonic and supermagnetosonic values avoid the presence of body modes, which are internal KH instabilities growing by resonant reflexion at the jet surface when the flow is sufficiently super-fast magnetosonic (Ferrari 1998). Body modes do not seem to play a major role in the disruption of jets. Moreover, the absence of these internal KH modes facilitates the interpretation of our results. Hence, as in most of the previously cited works, we are left with the surface KH modes. As the Alfvén number $M_{A,z}$ is equal to 6.52, we address the weak field regime defined in Ryu et al. (2000). Furthermore, we concentrate our analysis to a case study where the magnetic field is characterized by a small pitch length $P_i = rB_z/B_\theta$ as compared to the jet radius. Appl et al. (2000) have argued that this holds in most real astrophysical jets. Such current-carrying configurations are strongly unstable with respect to CD modes, which could interact with KH ones. Two other configurations having (i) a longer pitch length and (ii) no azimuthal field component serve as reference cases. The paper is organized as follows. The physical model and the numerical code are presented in §2. In section 3, we show the results of a linear stability study. Section 4 is devoted to the nonlinear numerical results. We conclude with discussing the consequences of our findings in the context of astrophysical jets.

2. The jet model and the numerical code

2.1. The unperturbed magnetized jet model

For simplicity, we consider equal density fluids, separated by a flow shear layer having an hyperbolic tangent profile with a small width compared to the jet radius. The cylindrical jet has an initial background flow directed along the axial direction and sheared in the radial one, given by

$$V_z(r) = \frac{V}{2} \tanh\left(\frac{R_j - r}{a}\right), \tag{1}$$

where (r, θ, z) cylindrical coordinates are used. The amplitude of the velocity shear is given by V, and the shear layer is situated at the jet radius R_j with a radial width given by the parameter a. Note that the jet surface is at rest: this choice of reference frame is well adapted to the study of the development of KH surface modes, as they have phase and group velocities given approximately by the local flow velocity, here zero. In the present study, we fix $V = 1.63$, $R_j = 1$, and $a = 0.1R_j = 0.1$. As we choose a uniform mass density $\rho = \rho_0 = 1$ and an axial gas pressure $p(r = 0) \equiv p_0 = 1$, the sound speed on axis is $c_s = (\gamma p_0/\rho_0)^{1/2} = 1.29$ for an adiabatic index $\gamma = 5/3$. The flow is then slightly supersonic with a sonic Mach number $M_s = V/c_s$ equal to 1.26 on axis. For the magnetic configuration, we consider an helical magnetic field defined as

$$B_r = 0, \;\; B_\theta = B_1 \frac{r/r_c}{1 + (r/r_c)^2}, \;\; B_z = B_0, \tag{2}$$

where B_0 and B_1 control the field amplitude and twist, and r_c is the characteristic length for its radial variation. For non zero B_1, the current density is correspondingly peaked on axis. In order to achieve a MHD equilibrium having a uniform mass density ρ_0, the magnetic field requires the following radial temperature variation,

$$T = T_0 - B_1^2/(2\rho_0)\left(1 - \frac{1}{[1+(r/r_c)^2]^2}\right), \tag{3}$$

where $T_0 = p_0/\rho_0$ is the temperature on axis. The magnetic permeability is equal to one in our dimensionless specifications. In a previous work on CD instabilities, a force-free configuration having a uniform pitch length has been taken (Appl et al. 2000). The present investigation has a radial variation of the pitch length which is parabolic and given by

$$P_i = \frac{r_c B_0}{B_1}[1+(r/r_c)^2]. \tag{4}$$

This choice has two advantages. It allows direct comparison with a uniform longitudinal field case, as the axial component is constant. Second, a non uniform pitch configuration is easier to handle numerically than a shear-free one, which is generally subject to numerical interchange instabilities.

As the azimuthal component of the magnetic field vanishes only at an infinite radial distance, the electric current flowing in the jet itself is non zero and a return current flowing back in the external medium is assumed. In this work, we use $B_1 = T_0 = 1$ and $B_0 = 0.25$. Consequently, we address the weak field regime as the initial Alfvén Mach number is $M_{A,z} = 6.52$. Note that the flow is only sligthly supermagnetosonic, as the fast magnetosonic Mach number taken on axis is $M_f = V/(c_s^2 + v_A^2)^{1/2} = 1.24$. Two helical configurations having a non zero current density and referred to as HEL1 and HEL2 are studied extensively in this work, corresponding to $r_c = 2$ and 0.5, respectively. These two cases have the same initial azimuthal magnetic field component at the jet radius R_j. A uniformly magnetized case, referred to as UNI, has a constant $B_z = 0.25$ and is retained to serve as reference case. All three cases have an axial plasma beta $\beta_0 = 2p_0/B_0^2 = 32$. The parameter values used in the different runs are listed in Table 1.

2.2. The Versatile Advection Code

The nonlinear simulation results are all obtained using the general finite-volume based Versatile Advection Code, VAC[1] (Tóth 1996). For the present study, we use the full set of

[1] See `http://www.phys.uu.nl/~toth`.

ideal compressible MHD equations. A three dimensional cartesian grid is employed. We select the explicit one-step total variation diminishing (TVD) scheme with Woodward limiting (Collela and Woodward 1984; Harten 1983). This is a second-order accurate shock-capturing method making use of a Roe-type approximate Riemann solver. We apply a projection scheme at every time step in order to remove any numerically generated divergence of the magnetic field (Brackbill and Barnes 1980).

We consider an idealized problem by assuming periodicity along the axial direction. The consequence is to restrict the allowed axial wavelengths λ to some Fourier components that can fit in the cylinder of length L, i.e. $\lambda = L/n < L$ with n a positive integer. The main influence of this choice on the results is to limit the large-scale coalescence of the structures as discussed by Frank et al. (1996). The jet configuration is set up in a cartesian (x, y, z) box of sizes $4R_j \times 4R_j \times L$. In this work, we use fixed boundary conditions at $x = y = \pm 2R_j$, in order to maintain the helical field at these boundaries. For a uniformly magnetized case, the choice of open (zero gradient) versus fixed conditions at these boundaries does not influence our evolution results up to the considered time intervals. For the aspect ratio of $L/R_j = 2$, the fastest linearly growing $m = \pm 1$ KH surface modes have an axial wavenumber $k_z R_j = 2\pi R_j/\lambda = \pi$ (see below) and thus exactly fit the simulation box (as $\lambda = 2R_j = L$). In our initial setup, we perturb the MHD equilibria only at these $m = \pm 1$ azimuthal wavenumbers, as they are suspected to play a crucial role in the jet survival. The computations are carried out at a grid resolution of $200 \times 200 \times 100$, and exploit OpenMP parallelism to run on multiple processors of the SGI Origin 3800.

3. Stability study

We start off with a stability analysis to characterize the properties of the different linearly unstable modes for the three chosen configurations. We used two independent ideal MHD stability codes, described in detail elsewhere (Appl and Camenzind 1992; Appl 1996; Appl et al. 2000; Nijboer et al. 1997). In both codes, an eigenvalue problem for an infinitely long cylindrical jet is solved using a normal mode expansion for the perturbed quantities of the form $f(r) \exp[i(m\theta + kz - \omega t)]$. In Appl and Camenzind (1992), a temporal approach is taken in the ZYLSPEK code where a complex frequency $\omega = \omega_r + i\Gamma$ and a real wavenumber k are considered. The linear growth rate Γ of a mode specified by the wavenumbers m and k is then obtained. In the LEDAFLOW program (Nijboer et al. 1997), one similarly fixes the wavenumbers m and k, but one can solve for all eigenvalues ω simultaneously (including both overstable and damped eigenmodes) by solving the eigenvalue problem using the QR algorithm. Below, we express all our results in time units of the isothermal radial sound travel time $\sqrt{\gamma}R_j/c_s$, where c_s is the sound speed taken on axis.

The first configuration – UNI – has a uniform longitudinal magnetic field with $B_z = B_0 = 0.25$. We report in Figure 1 the linear growth rate Γ of the $m = \pm 1$ modes as a function of the axial wavenumber k, for different magnetic field strengths B_0. The $m = +1$ and $m = -1$ branches are degenerate. As mentioned previously, these dispersion branches correspond to surface instabilities, while body modes are stable. The growth rate at a specified wavenumber k, for a weak field case like UNI, is very close to that of a purely hydrodynamic configuration. The effect of a weak axial magnetic field is almost negligible in the linear evolution of KH instabilities. Conversely, the growth rate is significantly reduced for higher field strengths like $B_0 = 0.6$, while $B_0 = 0.8$ is fully stabilized, as in that case $M_{A,z} \simeq 2$ and we enter the linearly stable regime.

The $m = \pm 1$ dispersion branches obtained for the helical configurations HEL1 and HEL2 are plotted in Figure 2. First, the helical field structure lifts the degeneracy between $m = +1$ and $m = -1$ modes. Indeed, the $m = -1$ KH linear growth rate dominates its $m = +1$ counterpart for a given unstable axial wavenumber k. Second, an additional dispersion branch having a $m = -1$ azimuthal mode number appears, with a growth rate that is even dominant for the HEL2 case. This latter instability is magnetic in nature. Indeed, this dispersion branch is quasi-unchanged when we investigate the stability of the same MHD equilibrium in a static configuration ($V = 0$), as also shown in Figure 2. Furthermore, the group velocity is drastically different for the two mode types: it is approximately zero for the KH branch while it is close to $V/2$ for the CD one. The results reported in Figures 1 and 2 using the ZYLSPEK code are in excellent agreement with those obtained with the LEDAFLOW program. For example, for the HEL2 case, the unstable ($m = -1, kR_j = \pi$) eigenvalues obtained from the LEDAFLOW code are $\omega = \omega_r + i\Gamma = -0.072 + i0.6769$ and $-2.559 + i0.8474$ while ZYLSPEK code gives $\omega = -0.065 + i0.6963$ and $-2.560 + i0.846$. Figure 3 shows the full slow and Alfvénic subspectrum computed with LEDAFLOW for all three cases for fixed wavenumbers $m = -1$ and $kR_j = \pi$. At about this axial wavenumber, the dispersion curve for the uniform configuration as shown in Figure 1 reaches its maximum. The KH instability is clearly distinguishable in all three spectra, while the CD type mode – although present for both HEL1 and HEL2 configurations – is dominant for the HEL2 case alone. The overview of the entire MHD spectrum of instabilities, waves and damped modes at fixed wavenumbers in Figure 3 also serves to show that the dominant linear response to wavenumber selected perturbations will not be dramatically influenced by other overstable modes than those of interest here. Finally, the radial component of the fluid displacement is plotted in Figure 4 for the three branches of the HEL2 case for a given $kR_j = \pi$. Note the internal character of the CD mode which primarily affects the jet core. This is in good agreement with results previously obtained on CD instabilities as in Figure 2 of Appl et al.

(2000). The displacements associated with the KH modes have a radically different radial variation and are essentially confined to the vicinity of the jet radius.

We can compare the CD growth rate values reported here with those predicted from previous work by Appl et al. (2000), where shear-free force-free equilibria were studied. There, it was obtained that the most unstable CD mode develops with a linear growth rate $\Gamma = 0.133 v_A/P_0$ when the axial pitch length $P_0 \ll R_j$, and v_A denotes the Alfvén velocity on axis. This predicts a Γ value of 0.27 for the HEL2 case, substantially smaller than the value 0.9 deduced from Figure 2. This apparent disagreement is explained by the differences between the two equilibrium configurations. In the force-free equilibria taken by Appl et al. (2000), the thermal pressure gradient is absent by definition, while in our configuration, the radial pressure variation leads to an extra destabilization. More precisely, the thermal pressure gradient raises the available energy to feed the instability via a second term, the first contributing term being a parallel current one in accord with the pitch value. In other words, the CD instability considered here is not purely current-driven but also partially pressure-driven. However, as the mode character does not differ significantly from a pure CD one, we will continue to speak of a CD instability below. For the HEL1 configuration, the normalized pitch length value $P_0/R_j = 0.5$ is close to one, so that CD modes are of lesser importance. Since the two helical configurations have the same value of the azimuthal magnetic field component at the jet radius $r = R_j$, we anticipate that it will be possible to separate (1) the effect of a prevailing local helical field on the KH development from (2) effects on the KH mode due to the additional development of a CD mode and their mutual interaction.

For completeness, we mention that many other modes having $m = 0, \pm 2, \pm 3, ...$ are also unstable with non negligible growth rates. As we directly excite the dominant $m = \pm 1$ perturbations, we only reported linear results for those modes. As a final note on the linear results, the stability calculations using the temporal approach employed a free boundary condition situated at $r = 2R_j$, while the LEDAFLOW code assumed a fixed boundary, as will also be done in the subsequent nonlinear studies from the following section. The quantitative agreement between both linear stability code results demonstrates that these are not sensitive to the position or the nature of this numerical boundary, as long as it is placed sufficiently far away from the jet surface. This is due to the radially localized character of the described perturbations.

4. Nonlinear results

The three configurations are perturbed by adding the following radial velocity profile

$$v_r = \delta V \exp - \left(\frac{r - R_j}{4a}\right)^2 \times \cos(m\theta) \ \times \sin\left(\frac{2\pi n z}{L}\right). \qquad (5)$$

We set $m = 1$ and $n = 1$ in the above formula in order to excite the four 2D Fourier modes $(m, n) = (\pm 1, \pm 1)$. Due to symmetry considerations between (m, n) and $(-m, -n)$ pairs, we can always refer to a (m, n) mode with $n \geq 0$. We impose a perturbation at $m = \pm 1$, since our interest here is to primarily focus on these modes. We take a $n = 1$ axial mode number, which corresponds to a wavenumber $kR_j = \pi$ close to the fastest linearly growing KH one, as can be seen in Figures 1 and 2. The amplitude of the perturbation is taken to be $\delta V = 0.01$, and its radial width is $4a = 0.2$. This perturbation easily excites surface KH modes. It also initiates CD instabilities, when they exist. Indeed, the perturbation given by equation 5 for $m = 1$ involves a small, but finite displacement of the jet axis, which turns out to be sufficient to trigger the growth of the CD modes. This is because they have a typical normal mode structure with a radial velocity component peaked on axis as shown in Figure 4.

4.1. Comparative Overview

Before examining in detail the simulation results, it is instructive to have a comparative overview of the time evolution in the three cases. This can be done by inspecting the mass density structure, as shown by snapshots at various times in Figures 5, 6, and 7, using a 2D vertical cut at $x = 0$ containing the jet axis. Since we normalized the grey scale range by the extremal values of density to bring out all detail in each simulation, the contour levels slightly differ from one figure to the next. The range of density values over all frames plotted in Figures 5, 6, and 7, is $0.60 \lesssim \rho \lesssim 1.27$.

First, at early times, a $n = 2$ KH vortical structure situated in the vicinity of the jet surface is clearly visible for the UNI case. This is due to a quasi-linear coupling effect between the initially perturbed $(m = 1, n = 1)$ and $(m = -1, n = 1)$ modes, which induced the excitation of secondary $(m = 0, n = 2)$ and $(m = 2, n = 2)$ modes (Keppens and Tóth 1999). These quasi-linear couplings were predicted by an analytic reasoning for the early stages in a pure hydrodynamic evolution. As long as the plasma beta is sufficiently high – the case studied in Keppens and Tóth (1999) had a uniform $\beta(t = 0) = 120$ while the UNI case here has $\beta(t = 0) = 32$ – these couplings occur in a precise ordering. The further evolution is then partially controlled by these secondary instabilities. In contrast, for the two helical configurations HEL1 and HEL2, Figures 6 and 7 demonstrate that the interface distortion is dominated by a $n = 1$ pattern. This morphological difference ensues from the linearly lifted degeneracy between the $m = \pm 1$ KH branches, which leads do the dominance of the $m = -1$ mode over the $m = 1$ one. The nonlinear coupling events leading to the excitation of secondary KH instabilities no longer occur, in line with the dynamical importance of the magnetic field at the jet radius from the very beginning. In fact, the initial local plasma beta at the jet radius turns out to be $\beta(R_j) = 7.37$ and 4.67 for the HEL1 and HEL2 cases, respectively. As a result, the KH evolution is significantly modified by the presence of an helical magnetic field, as compared to a uniform axial field case.

Second, for the HEL2 case, an additional pattern having a dominant $n = 1$ structure is also visible within the body of the jet. At early times, it appears as an internal helical layer of depleted density, which is well separated from the KH vortices. We can safely attribute this density perturbation to the development of a $(m = -1, n = 1)$ CD instability. This is substantiated by comparison with results obtained in an independent run, where the same MHD equilibrium was placed in a static configuration and a similar density disturbance developed. Furthermore, one can easily deduce from Figure 7 that, while the KH vortices are growing in place, the CD perturbation is advected along the jet axis at a speed of roughly $V/2 \approx 0.8$.

At later times, the overall evolution shows saturation and disruption stages in all three cases. However, since the interaction of CD and KH structures is visible at times leading to saturation for the HEL2 configuration, one can expect significant effects on the later stages as well. To that end, we compare in Figure 8 the time evolution of several characteristic quantities between the three cases. These are the volume averaged kinetic and perturbed magnetic energies restricted to the $x - y$ plane, i.e.

$$E^k_{xy} = \frac{1}{V_b} \int\limits_{V_b} \frac{\rho V_x^2 + \rho V_y^2}{2} \, dx dy dz \tag{6}$$

and

$$e^m_{xy} = \frac{1}{V_b} \int\limits_{V_b} \frac{B_x^2 + B_y^2}{2} \, dx dy dz - E^{m,0}_{xy}, \tag{7}$$

respectively, which are plotted in Figure 8a and 8b. V_b is the box volume, namely $V_b = 16 L R_j^2$. Similarly, one can find in Figure 8c the volume averaged axial total kinetic energy

$$E^k_z = \frac{1}{V_b} \int\limits_{V_b} \frac{\rho V_z^2}{2} \, dx dy dz, \tag{8}$$

and the axial perturbed magnetic energy

$$e_z^m = \frac{1}{V_b} \int\limits_{V_b} \frac{B_z^2}{2} \, dxdydz - E_z^{m,0}. \tag{9}$$

$E_{xy}^{m,0}$ and $E_z^{m,0}$ are the volume averaged magnetic energies obtained using the equilibrium components at $t = 0$. Additionally, Figure 8d shows the time history of the density contrast

$$\Delta\rho = \rho_{max} - \rho_{min}, \tag{10}$$

where ρ_{max} and ρ_{min} are the instantaneous maximum and minimum mass density values, as measured over the whole computational domain. The energetic quantities E_{xy}^k and e_{xy}^m allow the determination of the different evolutionary stages. In all three runs, the initial stage is characterized by an exponential growth in good agreement with the linear results plotted in Figures 1 and 2. The UNI and HEL1 growth rates are roughly the same, in accord with the fact that the dominant $m = -1$ mode for HEL1 has a similar growth rate than the $m = \pm 1$ pair for the UNI case. Also, the HEL2 growth rate is substantially smaller (by 17 per cent) than the one observed for the HEL1 and UNI cases, confirming that the initial growth is dominated by the $m = -1$ KH instability for the HEL2 equilibrium, as this instability is almost directly excited by the imposed perturbation. Note specifically how in this latter run, one can detect a sudden increase in the slope of the energies at time $t \simeq 8.5$. This can be attributed to the development of the dominant $m = -1$ CD instability for this configuration which is excited with a small time delay compared to the KH modes. Since the linear growth rate of the CD mode is larger than the KH one (see Fig. 2), it eventually contributes to the growth rate as deduced from the energy evolutions at intermediate times. To unambiguously identify the nonlinear saturation, we follow Keppens and Tóth (1999), who attribute the second or 'saturation' stage to the time corresponding to the first maximum in E_{xy}^k. Note in particular that E_{xy}^k and e_{xy}^m show maxima at times that differ slightly.

4.2. The Saturation

The physical mechanism responsible for the nonlinear saturation of the KH instability for a subsonic flow embedded in a uniformly magnetized configuration has been well described in two and three dimensional cartesian geometry by Jones et al. (1997) and Ryu et al. (2000), respectively. For completeness, we briefly recall their main results. Prior to saturation, the shear layer situated at the jet radius is rolling-up due to the development of vortical motions. As a consequence, the magnetic field lines are expelled from the center of the vortices. Meanwhile, the magnetic field is amplified by stretching and twisting in narrow filaments situated at the vortices perimeter. When the field strength becomes locally dominant, it thereby halts the growth of the instability and starts to control the further evolution. This saturation occurs in less than one turnover time of the vortex. For a subsonic cylindrical jet in a uniform magnetic field, the resulting structure at saturation has been described in detail by Keppens and Tóth (1999).

According to our definition, the saturation times are at $t \simeq 8$, 8.5, and 10 for the cases UNI, HEL1, and HEL2, respectively. It is instructive to compare the resulting density deformations at saturation, from the corresponding snapshots in Figures 5, 6, and 7 (the saturation time always corresponds to the panel on the second row, outmost left). Additionally, we also show a 2D $z = 1$ cut perpendicular to the jet axis at saturation in Figure 9. The latter figure again confirms that the KH density pattern has a morphological structure that is very different in helical cases as compared to a uniformly magnetized one. For example, contrary to the helical configurations, a $m = 3$ deformation dominates the jet cross-section structure in the UNI case. This, again, agrees with the nonlinear coupling events studied by Keppens and Tóth (1999), where a $(m = 3, n = 1)$ mode was observed at saturation. The $m = 3$ character of the jet deformation at saturation was found to be the result of cooperating thermal pressure variations and local amplifications in the initially weak and uniform magnetic field structure. Following the essentially hydrodynamic quasi-linear coupling effects mentioned in the previous section, sheet and fibril like field concentrations form and control the further jet surface deformations. The interaction of KH and CD perturbations can be seen in the HEL2 cross-section picture, although these density maps alone are slightly misleading as they suggest that the associated perturbations from KH and CD mode activity remain visually separated at saturation. Note however that the HEL2 vortical pattern has a smaller radial extent as compared to the HEL1 one. This is in favour of a stabilizing mechanism at work.

To quantify the difference in saturation behaviour between the different runs, we compare the saturation levels. The reduced kinetic energy E^k_{xy} of the HEL1 case reaches a maximal value of 0.014, which is much higher than for the UNI case where it is 0.009. This tendency is reversed for the perturbed magnetic energy e^m_{xy}, with values of 0.0065 and 0.0105 for the HEL1 and UNI cases, respectively. The summed energies quantifying the dynamics in the $x - y$ plane, $E^k_{xy} + e^m_{xy}$, are then 0.0195 for the uniform, versus 0.0205 for the helical HEL1 case, respectively. In the HEL2 run, one obtains a total perturbed energy of 0.014 $(0.012 + 0.002)$, a value which is 28 to 32 % reduced as compared to the previous two values. This lower value is indicative of a fairly effective suppression of transverse jet displacements.

We attempt to estimate the role of the additional CD instability in this different saturation behavior as follows. We start by noting that in the HEL2 case, the perturbed energies are the combined effect of two components, namely from the KH and the CD instability. To estimate the transverse $x - y$ dynamical effect of the CD component alone, we made an additional run where the same MHD equilibrium is placed in a static configuration. We then get values of 0.002 and -0.0035 for the energies E^k_{xy} and e^m_{xy}, respectively. Subtracting these values from the ones obtained in HEL2, this would imply a KH component of 0.0155 for the total perturbed energy of the HEL2 case. This value remains significantly smaller than for the two other configurations. We argue in what follows that a process based on an efficient stabilizing mechanism due to the presence of the CD instability can explain these quantitative differences and the overall lower saturation values.

Different mechanisms can lead to stabilization. A first mechanism could simply be the change in the local thermodynamic parameters induced by the CD perturbation. Recall that the growth rate of KH instabilities is substantially reduced for increasing Mach numbers. We first examined the changes associated with the depleted density region inside the jet core (see Fig. 7). A corresponding region of enhanced temperature is obtained, giving a local increase of the sound speed. This in turn decreases the Mach number and consequently would destabilize rather than stabilize. Moreover, the amplitude of this change is of order 20 %, which makes this process not efficient. In addition, the e-folding time associated with the linear growth rate is not fast enough as compared to the characteristic time of the local changes. Therefore, the stabilization is most likely of a magnetic origin.

Since CD modes nonlinearly redistribute the current density inside the jet core (Lery et al. 2000), we examined the magnetic deformation induced by the CD instability. The evolution of the current density associated with this particular CD magnetic deformation does not involve the development of a current sheet or current concentration layer. Therefore, we focused on morphologically identifiable regions in axial and azimuthal field maps. On the one hand, a region of a lowered axial field component coincidences with the depleted density region mentioned above. This would also destabilize. However, an opposite effect is found for the azimuthal field component, which is shown in Figure 10 for the two helical configurations. At this time, just prior to saturation, the comparison shows that, in the HEL2 case, an extended diffuse region of enhanced azimuthal field already invaded the jet surface surroundings. This perturbed field obtains a maximum value of order 0.75. The initial background azimuthal field value was 0.4 on the jet radius, indicating that a significant amplification of this component occured. This is in agreement with the fact that the free energy feeding the CD instability is provided by the azimuthal field. This field component is expelled from the jet core when meanwhile getting amplified to ensure flux conservation. When this augmented magnetic field component is carried outwards to the vortical structures, it helps to saturate the KH perturbations there. This process is effective before and during the self-saturation mechanism obtained in configurations without CD modes, and would explain the lower saturation level of the perturbed energies.

4.3. The Disruption and Mode Cannibalism

Beyond saturation, the KH vertical structures are first deformed. This is illustrated for the three runs in Figures 5, 6, and 7, where an elongation of the cat's eye pattern along the axial direction can be clearly seen. Meanwhile, the partial kinetic energy E^k_{xy} begins to decrease and the perturbed magnetic energies e^m_{xy} and e^m_z attain maximum values. At that point, the disruption of the vortices due to magnetic reconnection occurs (i.e. at time $t \simeq 10, 10.5, 12$ for the UNI, HEL1, and HEL2 cases, respectively) and the magnetic and kinetic energies stored during the early stages are then released. This is the same effect previously described for uniform longitudinal field configurations. Clearly, an effective numerical resistivity is necessary to allow magnetic reconnection to occur during the disruption stage. In the simulations presented here, we rely on the numerical resistivity associated with the finite grid resolution employed. One then generally hopes that a sufficiently small dissipation can be achieved in order to correctly simulate the limit regime of high kinetic and magnetic Reynolds numbers (see discussion in Jones et al. 1997). For astrophysical plasmas in magnetized jet conditions, the true physical dissipation is likely to be much smaller than the present one which is due to the grid resolution. In the phases prior to the disruption, a sufficient resolution to resolve the ideal nonlinear dynamics must be employed (the instabilities considered here are ideal MHD modes). To check whether the nonlinear saturation stage is adequately captured, and to investigate how the results in the disruption stage depend on the dissipative scales allowed in the simulations, we repeated all three runs using five different grid resolutions from $100 \times 100 \times 50$ up to $200 \times 200 \times 100$. Figure 11 shows the time evolution of the reduced kinetic energy E^k_{xy} for the HEL1 and HEL2 cases. The results of the UNI case (not plotted) show a resolution dependence similar to HEL1. Notably the HEL2 results are more resolution dependent than the HEL1 ones. When inspecting 2D cuts of the mass density at saturation of the various resolution HEL2 runs, one finds that the KH vortices appear weaker and nearly not form at $100 \times 100 \times 50$, while they clearly develop in the higher resolution runs. On the other hand, the CD perturbation pattern is always well developed at all five resolutions. To some extent, one could argue that this again indicates that KH perturbations are strongly stabilized. Stabilization is enhanced at lower resolution because the corresponding enhanced dissipation broadens the KH and CD perturbed regions, making the spatial interaction between both instabilities more effective.

As far as the stage beyond saturation is concerned, our convergence study does indicate that, for the two helical cases, the further evolution is characterized by a continuous decay of the kinetic and magnetic energies. For the UNI case, there is a noticeable difference as a second maximum in E^k_{xy} is reached. This probably corresponds to the formation and disruption of several weaker secondary vortices. All simulations stop at time $t = 14$, since the resolution used in this study does not allow us to simulate in quantitative detail the later stages, as those will be dominated by numerical diffusion and probably end up in a fairly laminar stationary state. We can nevertheless quantitatively address the fine-scale structure which develops during the disruption. This is done by plotting the time evolution of the volume integrated square vorticity (enstrophy) reduced to the $x - y$ plane,

$$\Omega^2_{xy} = \frac{1}{V_b} \int\limits_{V_b} (\nabla \times V)^2_x \; + (\nabla \times V)^2_y \; dxdydz, \tag{11}$$

which is plotted in Figure 12. Note that both helical configurations lead to a square vorticity attaining a level that is significantly lower than for the UNI case. This is substantiated by Figure 13 showing snapshots of the density at the end of the run at $t = 14$. One sees that the mass density exhibits a turbulent nature for the uniformly magnetized case which is much less pronounced in the two other cases. The hoop force of the helical field succesfully suppresses the turbulent cascade towards small scales in the HEL1 and HEL2 cases. The current density (not shown) also confirms this tendency for the formation of small scale magnetic structures. An impression of the 3D jet structure at the end of our simulations is given in Figure 14. Note how both helical configurations still have an identifiable jet boundary.

It is difficult to assess the effect of CD perturbations on the further evolution beyond the saturation stage. Nevertheless, at the end of the runs, the free axial kinetic energy feeding the KH perturbations has much less decreased for the HEL2 case than for the two other ones as shown in Figure 8. This indicates that the initial background flow is less affected, and as a result will be less disrupted when a final stationary state is attained. Conversely, one can ask the question of how, in turn, the perturbations attributable to the CD instability are affected by the vortices disruption. During the disruption phase just after the saturation, the density contrast that is shown in Figure 8d, attains a level that is four times higher for the HEL2 run than in the two other ones. This must be associated with the CD instability which considerably enhances it through the formation of additional depleted and locally enhanced density regions. However, at the end of the simulation, a sudden drop is observed and the density contrast returns to a level comparable to the two other cases. The visual impression obtained from animations of various cross-cuts, like the sequence of images shown in Figure 7, lead us to suggest that the CD pattern has been 'gobbled up' by KH vortices and gets completely entangled and disrupted in the process. This type of mode-mode interaction evokes the terminology of "mode cannibalism".

5. Summary, outlook and astrophysical relevance

Previous studies have shown how a weak uniform magnetic field parallel to the jet flow configuration leads to important modifications of the nonlinear evolution of KH instabilities, compared to a pure hydrodynamic case. In this so-called weak field regime, the dissipation and associated turbulence occuring beyond disruption of the vortices are reduced. This makes KH instabilities less disruptive to the flow and ameliorates the jet survival, which is a major problem in astrophysical jet context.

In this work we account for the fact that far from the source, astrophysical jets possess an helical magnetic field with a non negligible azimuthal component eventually dominating the axial one. Besides being subject to KH instabilities, such current-carrying configurations are strongly unstable to magnetic modes, which originate in the electric current parallel to the magnetic field. While at first sight, the presence of such additional instabilities would worsen the problem of jet coherency, our detailed analysis of their nonlinear interaction has indicated that it aids in stabilizing the jet structure. The focus of this work is the interaction between both types of instabilities and how they affect the evolution of the jet configuration. To this aim, we considered three MHD equilibria having the same constant axial field component which magnitude is taken to be weak in order to assess the weak field regime. A case with a vanishing azimuthal field component served as a first reference case. A second configuration having an azimuthal component with a rather high pitch length in order to avoid the development of CD modes is also considered. The central configuration of interest in this work, had an helical field equilibrium in which CD modes are strongly unstable due to the relatively small pitch of the field lines. As the latter two cases where selected to have the same azimuthal field strength at the jet radius, we could separate the effects due to the presence of a background helical field from those due to additional magnetic instabilities. The structure of the flow was chosen as simple as possible in order to represent an idealized cylindrical jet. A supersonic case was considered, but the magnitude of the velocity difference between the jet and the ambient medium was taken to be relatively small to avoid the development of KH body instabilities.

We can summarize our findings as follows. First, in the three configurations, KH perturbations linearly develop at the specified excited wavenumbers in quantitative agreement with ideal stability results. In the two helical cases, this linear stage is characterized by the dominance of the $m = -1$ mode over its $m = 1$ counterpart. This lifted degeneracy compared to the uniform case leads to clear morphological differences of KH vortices developing at the jet surface in the further nonlinear evolution. In the CD unstable helical case, an additional $m = -1$ mode that is mainly driven by the electric current is observed to develop after some time delay. It affects primarily the jet body and has an associated depleted helical density region. In all three cases, a nonlinear saturation stage is obtained. We showed how the saturation is modified by the presence of a CD mode. In particular, a stabilizing nonlinear interaction mechanism was identified. The CD instability induces a diffuse region of enhanced azimuthal field B_θ, which invades the KH vortical structures and acts to stabilize. The saturation level of the KH perturbations and the energy extracted from the free background kinetic energy are substantially smaller, as compared to the two other cases. The further evolution is characterized by the disruption of the patterns in the three cases. In the two helical configurations, the formation of small scales is clearly reduced as compared to the uniform one. We are led to conclude that configurations having an helical field are less disruptive to the flow, especially when CD modes are present.

Despite the idealized configuration, our work represents a constructive step towards a better understanding of the nonlinear evolution of MHD instabilities in jets. A next step could be to explore a larger parameter region for the configuration, as appropriate for the fair variety of astrophysical jets. For example, in some MHD equilibria, a current layer or even a current sheet could form as a result of the nonlinear evolution of CD perturbations (Lery et al. 2000). The subsequent interaction with KH modes could be very different from the one obtained in this work. Indeed, configurations with 2D planar current-vortex sheets in which initial magnetic and velocity shear layers coincide have been studied previously. Keppens et al. (1999) demonstrated how an initial current layer can be deformed and amplified by KH vortices, leading in turn to secondary reconnection events and a transition to magnetically controlled turbulence. One could also study the compressible counterparts in similar current-vortex configurations of the ideal instabilities studied in incompressible MHD by Dahlburg, Boncinelli, & Einaudi (1997). Finally, the nonlinear evolution of KH modes can be affected by an initially asymmetric current sheet (Jeong et al. 2000). Future studies should focus on the highly supersonic regime, as is the case in most astrophysical jets, and explore random excitation of many linearly unstable modes. A recent study by Miura (1999) for 2D configurations with a magnetic field perpendicular to the flow, has observed the pairings of successive vortices. It would be of interest to investigate this for 3D cylindrical jet configurations.

The present results could help to reduce the discrepancy between observations of extended coherent astrophysical jets and the outcome of detailed stability studies. Recall that the very high resolution 3D hydrodynamic simulations by Bodo et al. (1998) were unable to reproduce the remarkable stability deduced from observations. Attempts to stabilize such supersonic jets without resorting to magnetic fields invoke jet densities much higher than that of the surrounding medium and/or favorable radiative effects (critically dependent on the choice of the cooling function) (Downes & Ray 1998, Micono et al. 2000, Stone, Xu, & Hardee 1997). Recent full 3D MHD simulations of supermagnetosonic jets have explored the effects of non uniform magnetic fields (Hardee, Clarke, & Rosen 1997; Rosen, Hardee, & Clarke 1999). Those studies confirm that in configurations having a significant azimuthal magnetic field, jets are able to propagate without disruption over a distance much larger than their radial extent. However, the same studies aim to describe the whole jet, and necessarily sacrifice resolution and are typically limited to capture axial length scales larger than $R_j/7$, while our local treatment has an axial resolution up to $R_j/50$. Since CD modes preferentially grow at high axial wavenumbers, their development and the interactions studied here are probably not well captured. Our results can also help to understand the morphological dichotomy in observed extragalactic jets. Fanaroff-Riley type I (FRI) jets appear turbulent and plume-like, losing their collimation after a relatively short distance. On the other hand, the FRII jets remain well collimated while propagating out to large distances and terminating in a strong shock. These differences can be explained by the different stability properties exhibited by the two classes. It is generally suggested that the remarkable stability of FRII jets is due to higher jet density and/or higher jet velocity, as compared to FRI ones. Our results also suggest that FRI objects could have a magnetic structure with a dominant axial field, while FRII ones could carry high electric currents.

Beside the issue of jet survival, many papers attempt to relate morphological features observed in jets to the development of KH instabilities. Succesfull examples include the possible interpretation for the origin of the emission knots that are clearly visible in some Herbig Haro stellar objects, by the nonlinear evolution of the $m = 0$ body mode (Micono et al. 1998) or by the interaction of various helical body modes (Xu, Hardee, & Stone 2000). In a very recent study, a mechanism based on the development of the $m = 0$ pinch mode in conically expanding, trans-Alfvénic jets embedded in a magnetized wind, has been identified to trigger a knotty structure (Hardee and Rosen 2002). Another example is given by the large-scale sinusoidal distortion observed in the 3C449 AGN jet, which has been attributed to the growth of the helical KH mode (Hardee, Cooper, & Clarke 1994). Observations from the Hubble space telescope of several protostellar systems have additionally revealed a finer scale structure with helical filaments and asymmetric knots (Heathcote et al. 1996). It is conceivable that CD instabilities with axial wavelengths that are much smaller than typical KH ones, can play a role in the observed jet structure at these smaller scales.

In conclusion, helically magnetized jets with significant azimuthal field components will likely be subject to both KH and CD instabilities. Their nonlinear interaction, as demonstrated in this paper, can aid in jet survival. Large-scale magnetic deformations associated with CD mode development can effectively saturate KH surface vortices and prevent jet disruption. The relatively short axial wavelengths for dominant CD modes calls for local, high resolution treatments. In first instance, such studies can neglect the effects of conical jet spreading and axial jet speed variation. Future, scale encompassing extensions of this work may provide further insight into both small, intermediate and large scale structures as observed in specific astrophysical jets.

This work was supported in part by the European Community's Human Potential Programme under contract HPRN-CT-2000-00153, PLATON. RK did the work under the Euratom-FOM Association Agreement and in the Computational Science programme 'Rapid Changes in Complex Flow' funded by NWO-E, coordinated by J.P. Goedbloed. HB thanks J.P. Goedbloed for his hospitality during his visit to the FOM institute. We are grateful to J. Heyvaerts for helpful discussions, and to S. Appl for letting us use his stability code. NCF is acknowledged for computing facilities. We thank the anonymous referee for useful suggestions.

REFERENCES

Appl, S., and Camenzind, C. 1992, A&A, 256, 354

Appl, S. 1996, A&A, 314, 995

Appl, S., Lery, T., and Baty, H. 2000, A&A, 355, 818

Begelman, M.C. 1998, ApJ, 493, 291

Birkinshaw, M. 1991, in Beams and jets in Astrophysics, p. 279, ed P.A. Hugues, Cambridge Univ. Press

Bodo, G., Rossi, P., Massaglia, S., Ferrari, A., Malagoli, A., and Rosner, R. 1998, A&A, 333, 1117

Bodo, G., Massaglia, S., Rossi, P., Rosner, R., Malagoli, A., and Ferrari, A. 1995, A&A, 303, 281

Brackbill, R.B., and Barnes, D.C. 1980, J. Comput. Phys., 35, 426

Collela, P., and Woodward, P.R. 1984, J. Comput. Phys., 54, 174

Dahlburg, R. B., Boncinelli, P., & Einaudi, G. 1997, Physics of Plasmas, 4, 1213

Downes, T.P., and Ray, T.P. 1998, A&A, 331, 1130

Ferrari, A. 1998, Annual Rev. Astrophys., 36, 539

Frank, A., Jones, T. W., Ryu, D., and Gaalaas, J. B. 1996, ApJ, 460, 777

Hardee, P. E., Cooper, M.A., Clarke, D. A. 1994, ApJ, 424, 126

Hardee, P. E., Clarke, D. A., and Rosen, A. 1997, ApJ, 485, 533

Hardee, P. E., and Rosen, A. 2002, preprint (astro-ph/0205377)

Harten, A. 1983, J. Comput. Phys., 49, 357

Heathcote, S., Morse, J., Hartigan, P., Reipurth, B., Schwartz, R.D., Bally, J., and Stone, J.M. 1996, AJ, 112,1141

Jeong, H., Ryu, D., Jones, T. W., and Frank, A. 2000, ApJ, 529, 536

Jones, T. W., Gaalaas, J. B., Ryu, D., and Frank, A. 1997, ApJ, 482, 230

Kersalé, E., Longaretti, P.-Y., and Pelletier, G. 2000, A&A, 363, 1166

Keppens, R., Tóth, G., Westerman, R.H.J., and Goedbloed, J.P. 1999, J. Plasma Physics, 61, 1

Keppens, R., and Tóth, G. 1999, Physics of Plasmas, 6, 1461

Lery, T., Baty, H., and Appl, S. 2000, A&A, 355, 1201

Malagoli, A., Bodo, G., and Rosner, R. 1996, ApJ, 456, 708.

Micono, M., Massaglia, S., Bodo, G., Rossi, P., and Ferrari, A. 1998, A&A, 333, 1001

Micono, M., Bodo, G., Massaglia, S., Rossi, P., Ferrari, A., and Rosner, R. 2000, A&A, 360, 795

Miura, A. 1999, J. Geophys. Res., 104, 395

Nijboer, R.J., van der Holst, B., Poedts, S., and Goedbloed, J.P. 1997, Comput. Phys. Commun., 101, 39

Rosen, A., Hardee, P. E., Clarke, D. A., and Johnson, A. 1999, ApJ, 510, 136

Ryu, D., Jones, T. W., and Frank, A. 2000, ApJ, 545, 475

Stone, J.M., Xu, J., and Hardee, P. E. 1997, ApJ, 483, 136

Tóth, G. 1996, Astrophys. Lett. Commun., 34, 245

Xu, J., Hardee, P. E., and Stone, J. M. 2000, ApJ, 543, 161

This preprint was prepared with the AAS LaTeX macros v5.0.

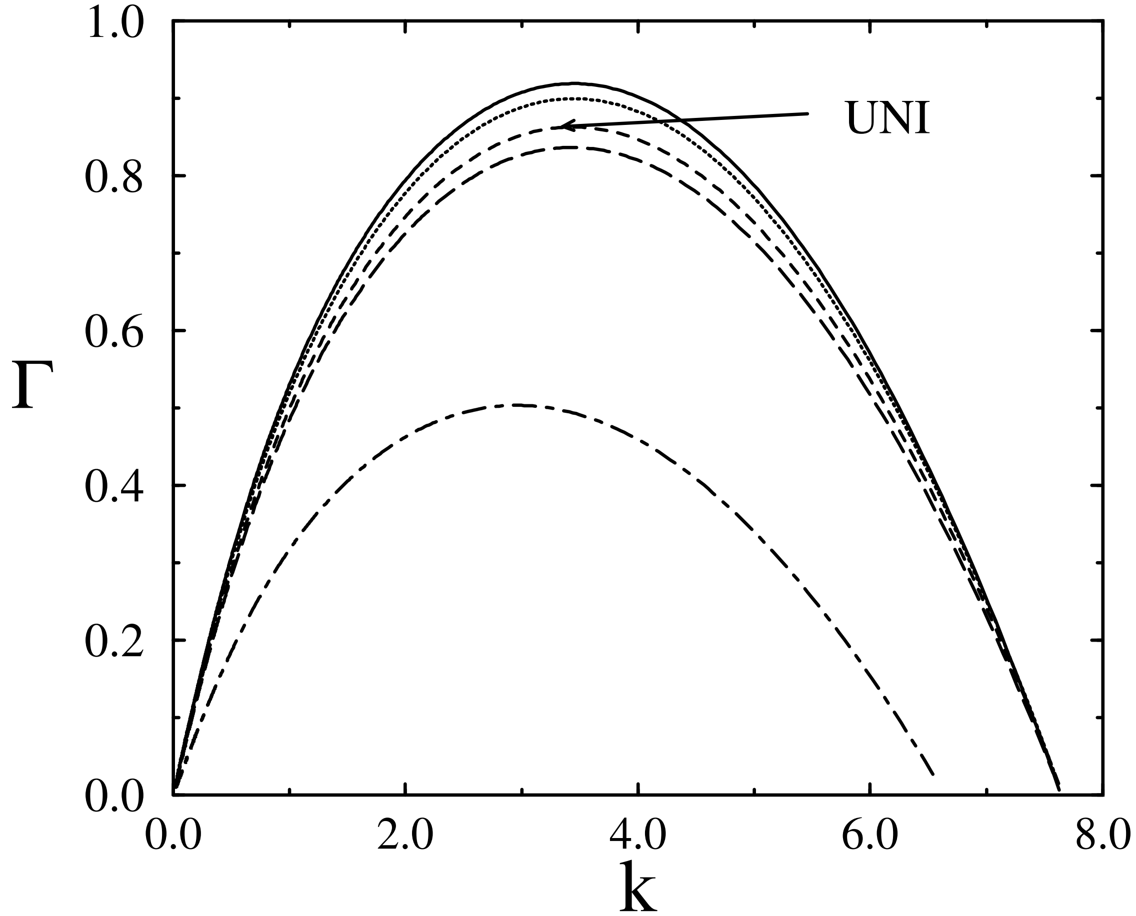

Fig. 1.— Linear growth rate $\Gamma(k)$ of $m = \pm 1$ modes for uniformly magnetized configurations having an axial field strengh B_0. Shown cases have $B_0 = 0.01$ (solid), $B_0 = 0.15$ (dotted), $B_0 = 0.25$ (short dashed), $B_0 = 0.3$ (long dashed), $B_0 = 0.6$ (dash-dotted). $B_0 = 0.8$ case is stable. Note that $m = -1$ and $m = +1$ branches are degenerate. The results are obtained using the ZYLSPEK code.

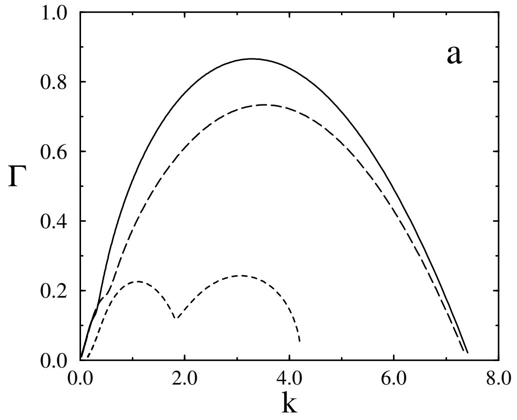

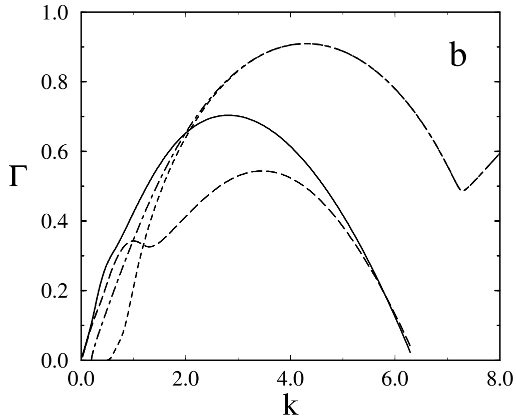

Fig. 2.— Same as Fig. 1 for the HEL1 (a) and HEL2 (b) cases. Shown are the $m = -1$ KH (solid), $m = 1$ KH (long dashed), and $m = -1$ CD (short dashed) dispersion branches. Also shown is the $m = -1$ CD (dash-dotted) branch obtained for an equilibrium similar to HEL2 but static ($V = 0$). The results are obtained using the ZYLSPEK code.

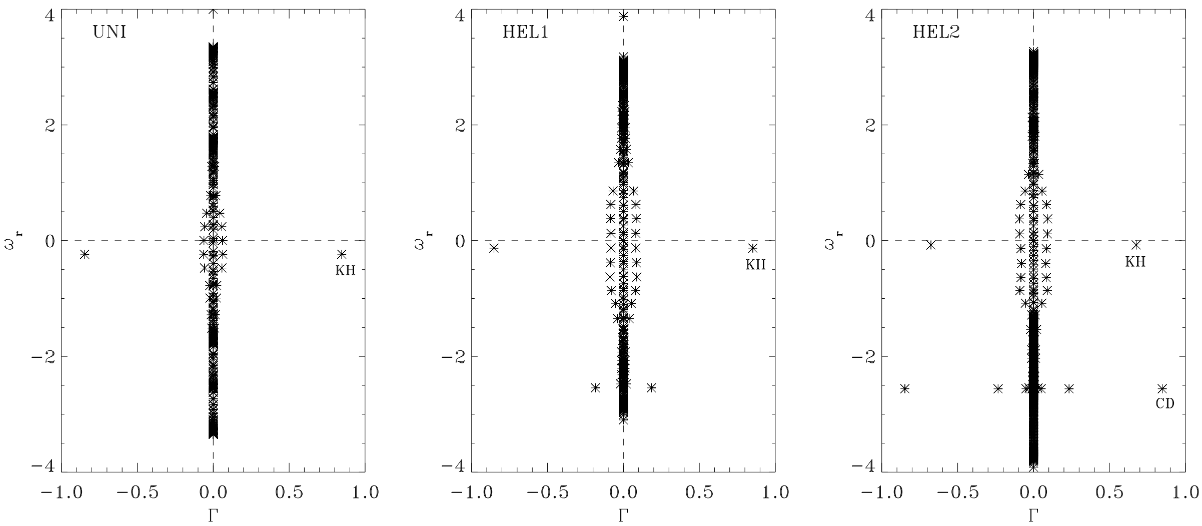

Fig. 3.— The full slow and Alfvén subspectrum at mode numbers $m = -1$ and $k = \pi$ for the three equilibrium configurations, obtained using the LEDAFLOW code.

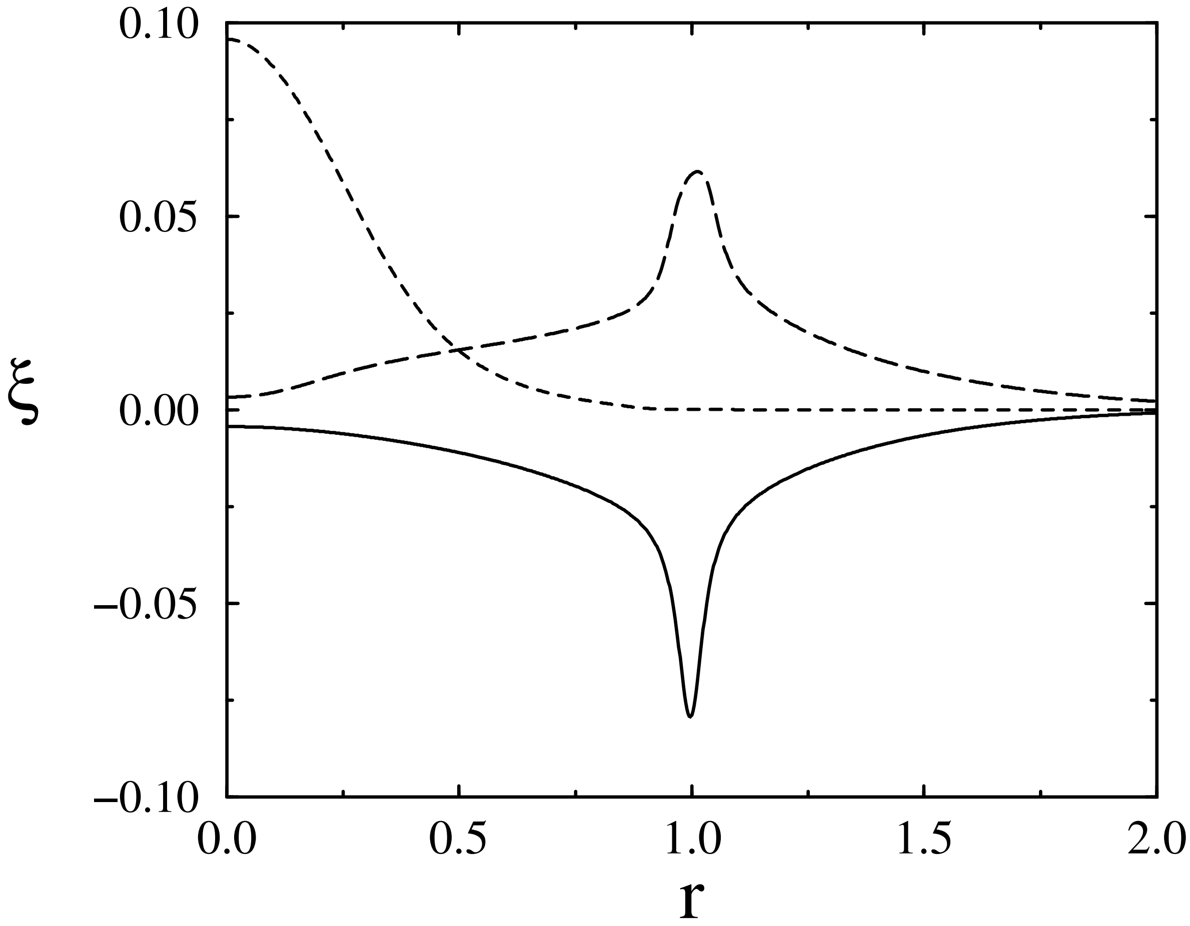

Fig. 4.— Radial variation of the radial component of the linear displacement $\xi_r(r)$. Shown are the $m = -1$ KH (solid), $m = 1$ KH (long dashed), and $m = -1$ CD (short dashed) modes at $k = \pi$. The jet radius is located at $r = R_j = 1$. The ZYLSPEK code is used.

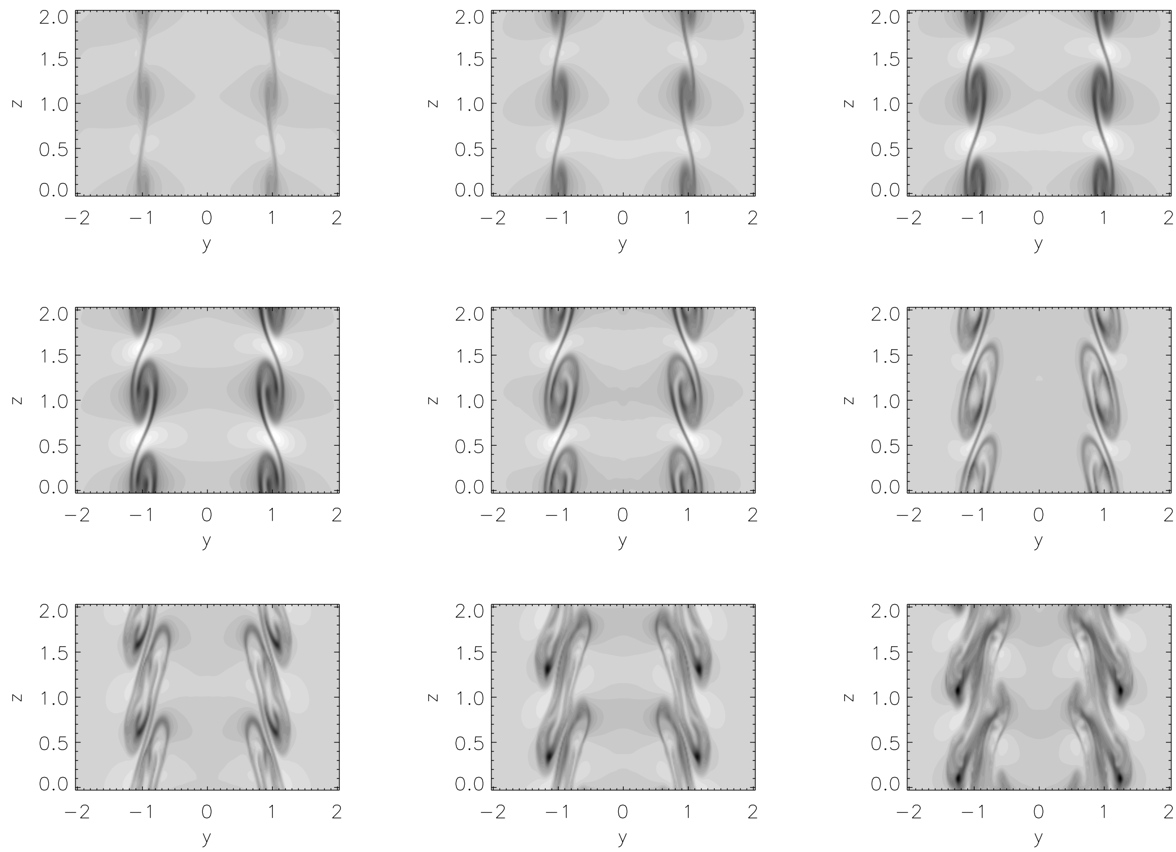

Fig. 5.— Grey scale images of the density distribution for the UNI case in the $y - z$ plane (using a 2D cut at $x = 0$). The times are $t = 6.5, 7, 7.5, 8, 8.5, 9, 9.5, 10, 10.5$, running from left to right and top to bottom. Dark regions correspond to low values.

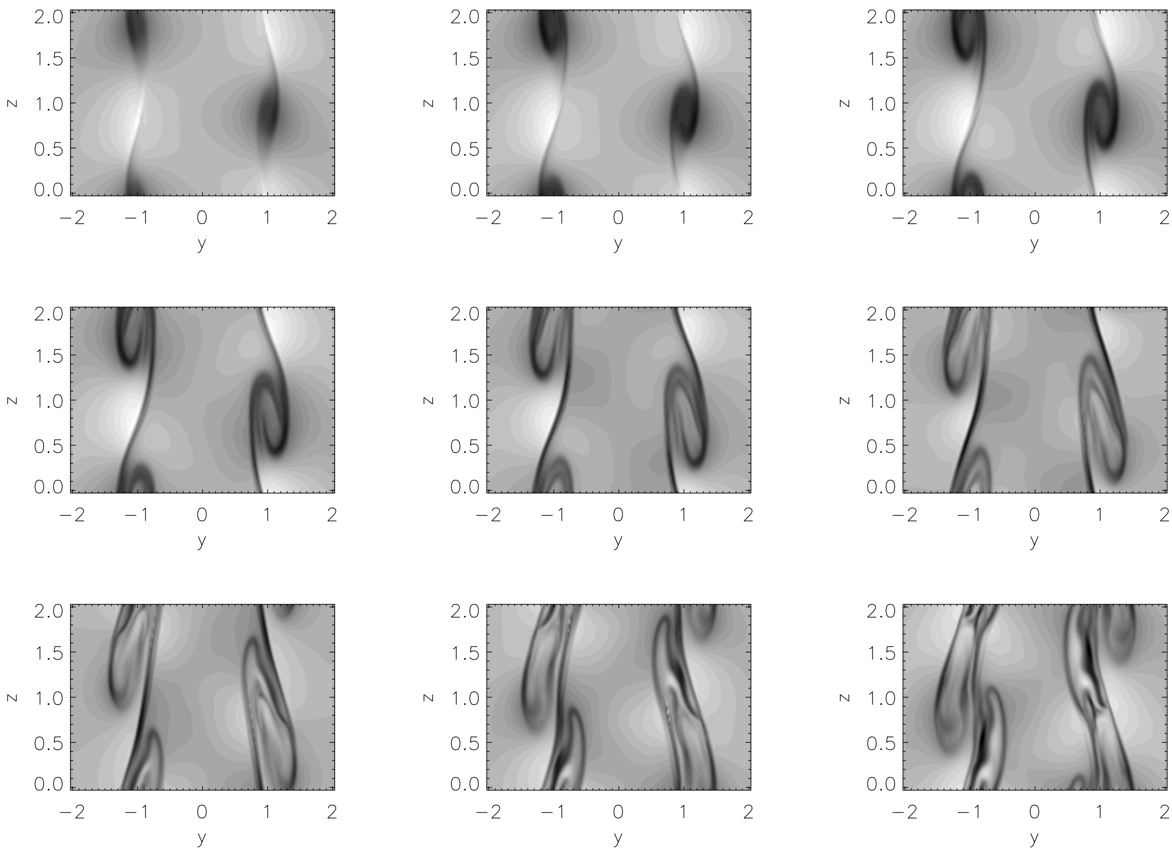

Fig. 6.— Same as Fig. 5, but for the HEL1 case. The times shown are $t = 7, 7.5, 8, 8.5, 9, 9.5, 10, 10.5, 11$, from left to right and top to bottom.

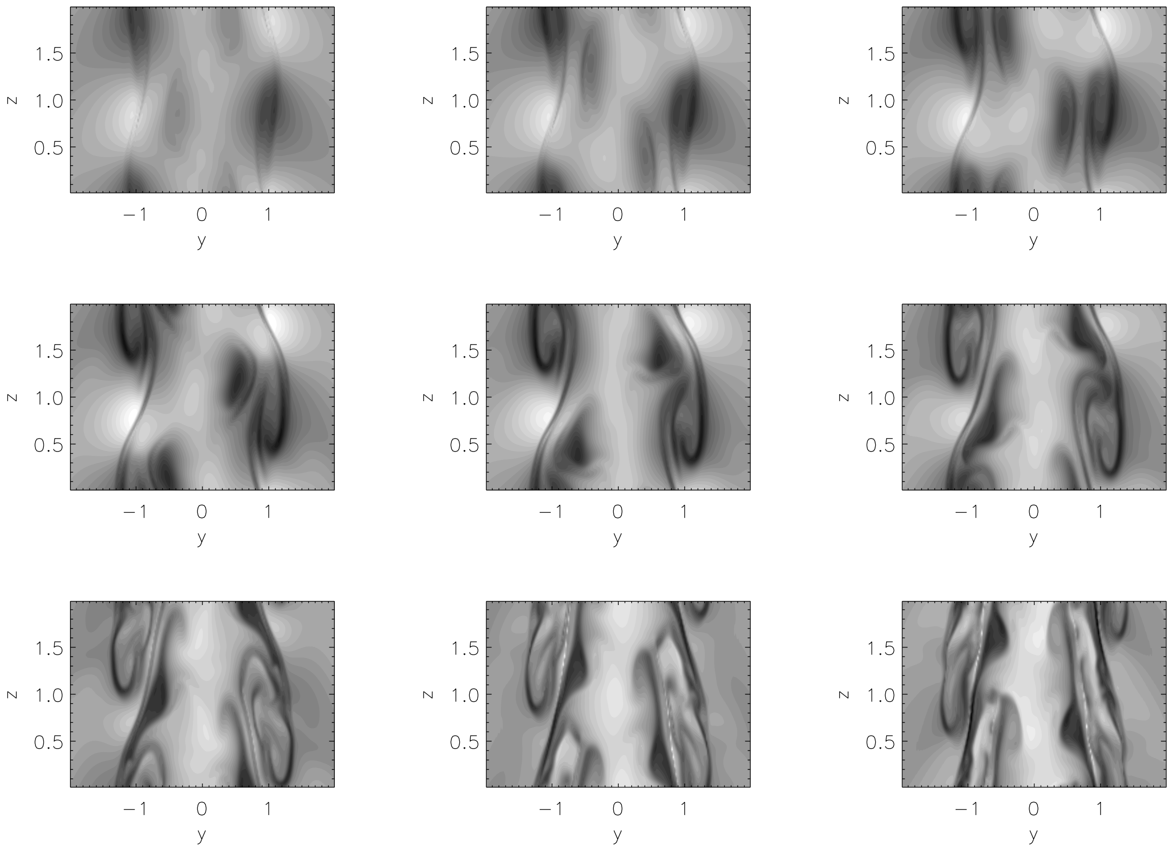

Fig. 7.— Same as Figs. 5-6, but for the HEL2 case. The times shown are $t = 8.5, 9, 9.5, 10, 10.5, 11, 11.5, 12, 12.5$.

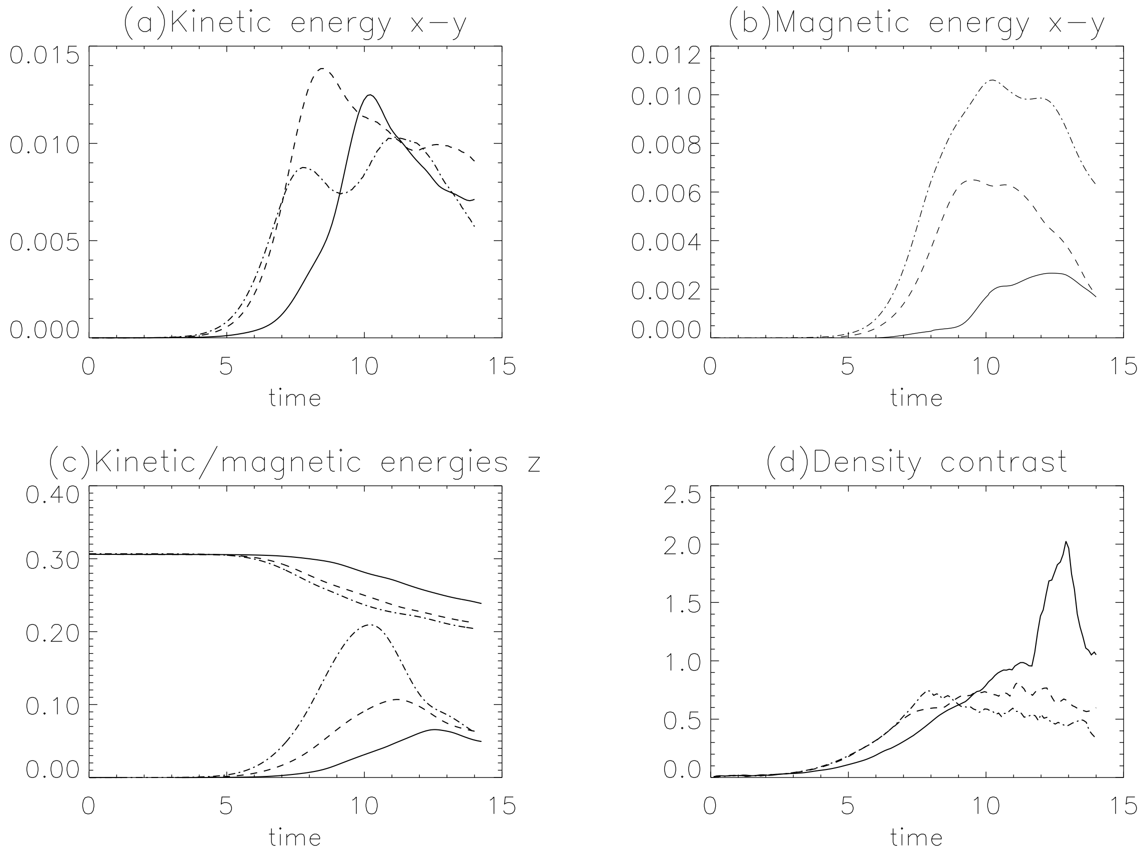

Fig. 8.— Time evolution of characteristic quantities in the UNI (dash-dotted), HEL1 (dashed), and HEL2 (solid) cases. Shown are the reduced kinetic energy E^k_{xy} (a), the perturbed magnetic energies e^m_{xy} (b) and e^m_z (three lower curves in c), and the total axial kinetic energy E^k_z (three upper curves in c). Note that e^m_z is multiplied by a factor 12 in order to be comparable to E^k_z on the plot (c). In addition, panel (d) shows the evolution of the density contrast $\Delta\rho$.

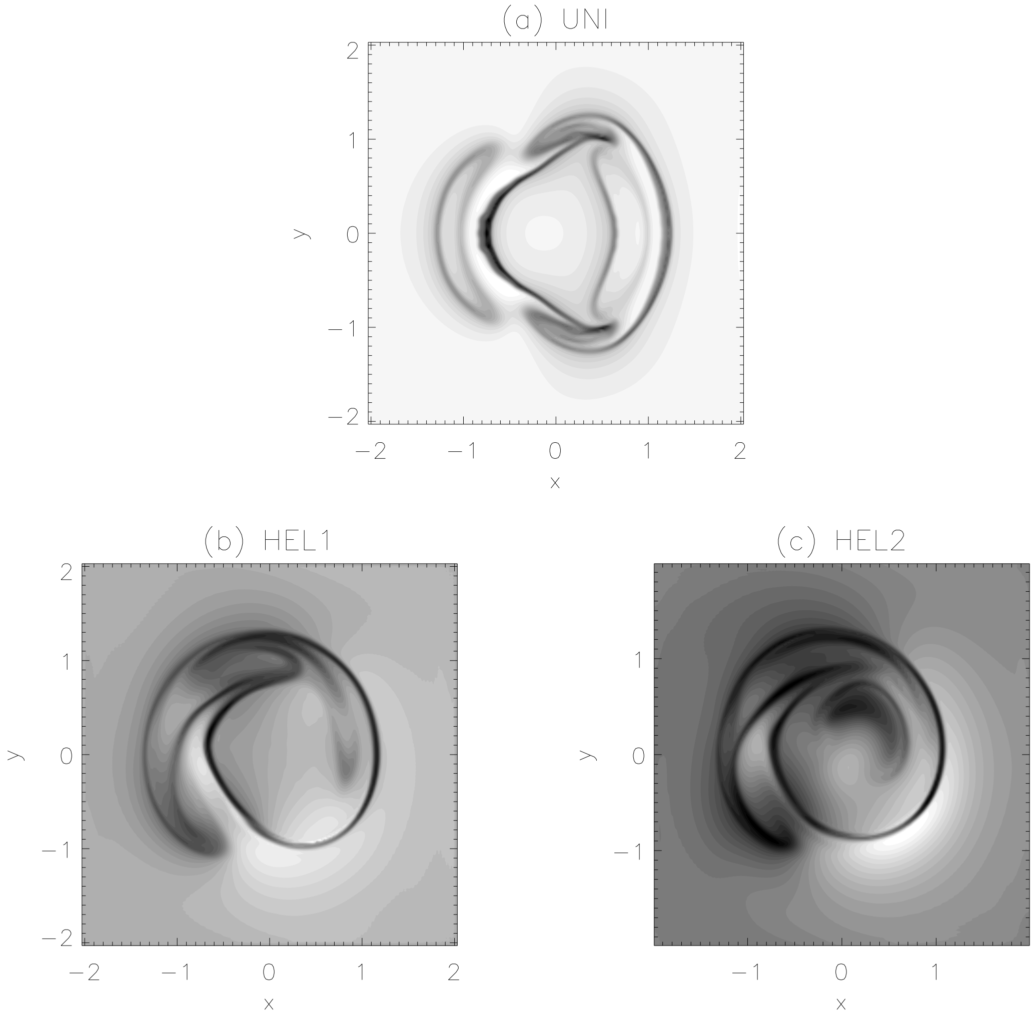

Fig. 9.— Grey scale images of the density distribution in the $x-y$ plane (using a 2D cut at $z=1$). Shown are the UNI (a), HEL1 (b), and HEL2 (c) cases at saturation. The contour levels are normalized using a linear scale with density values ranging from 0.51 to 1.31. The direction of the magnetic twist is clockwise for the helical runs.

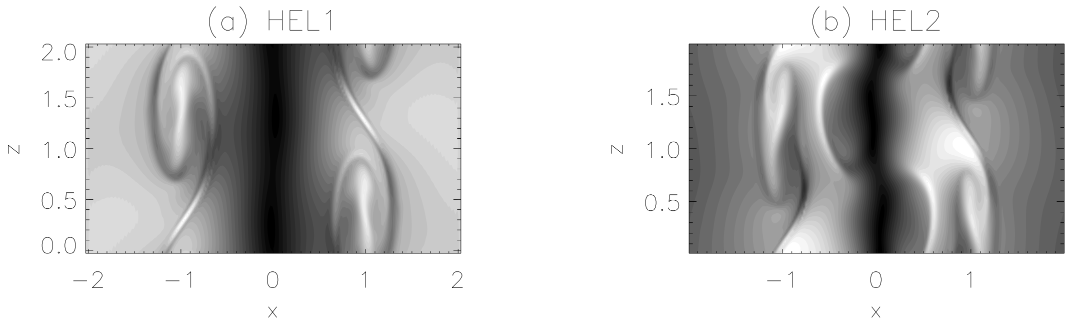

Fig. 10.— Grey scale images of the azimuthal field component B_θ in the $x - z$ plane (using a 2D cut at $y = 0$), at time $t = 8$ for HEL1 case (a), and at time $t = 9.5$ for HEL2 case (b). The contour levels are normalized using a linear scale with values ranging from 0.003 to 0.7. Dark regions correspond to low values.

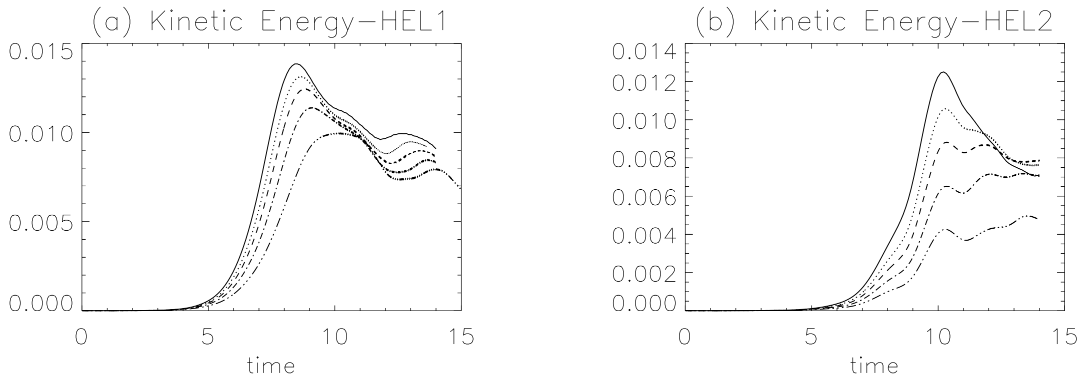

Fig. 11.— Time evolution of the perturbed kinetic energy E^k_{xy} for the HEL1 (a) and HEL2 (b) cases. The solid, dotted, dashed, dash-dotted, and long dash-dotted lines correspond to $200^2 \times 100$, $160^2 \times 80$, $140^2 \times 70$, $120^2 \times 60$, and $100^2 \times 50$ grid resolutions, respectively.

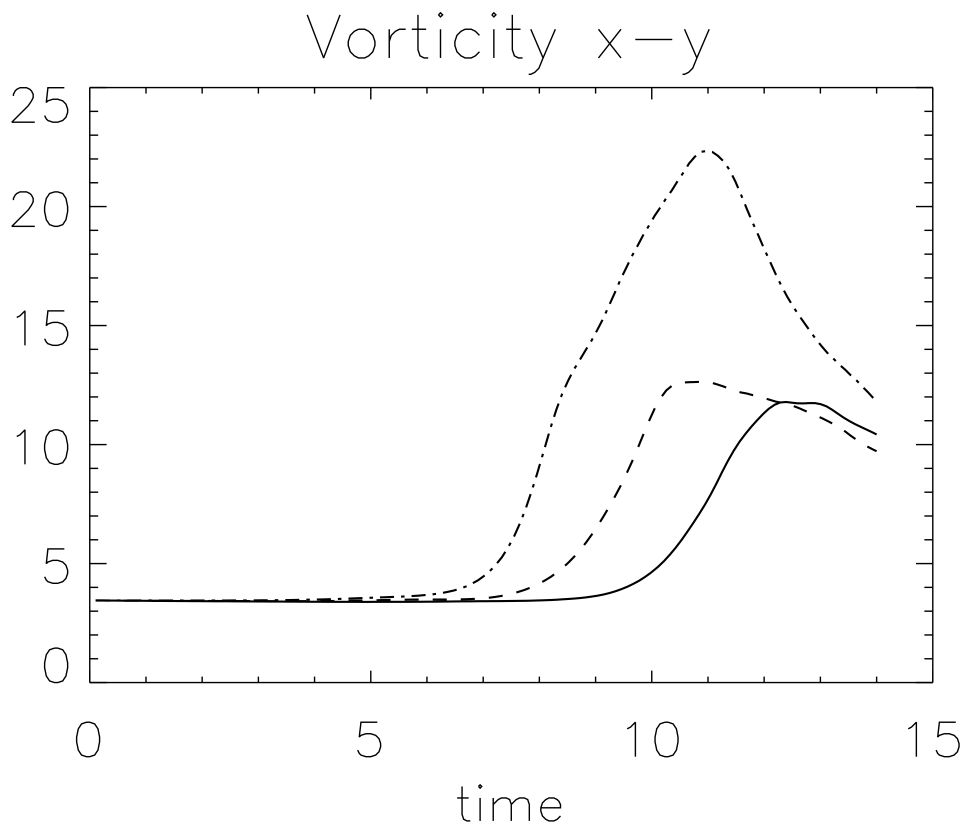

Fig. 12.— Time evolution of the reduced square vorticity Ω^2_{xy} for cases UNI (dash-dotted), HEL1 (dashed), and HEL2 (solid).

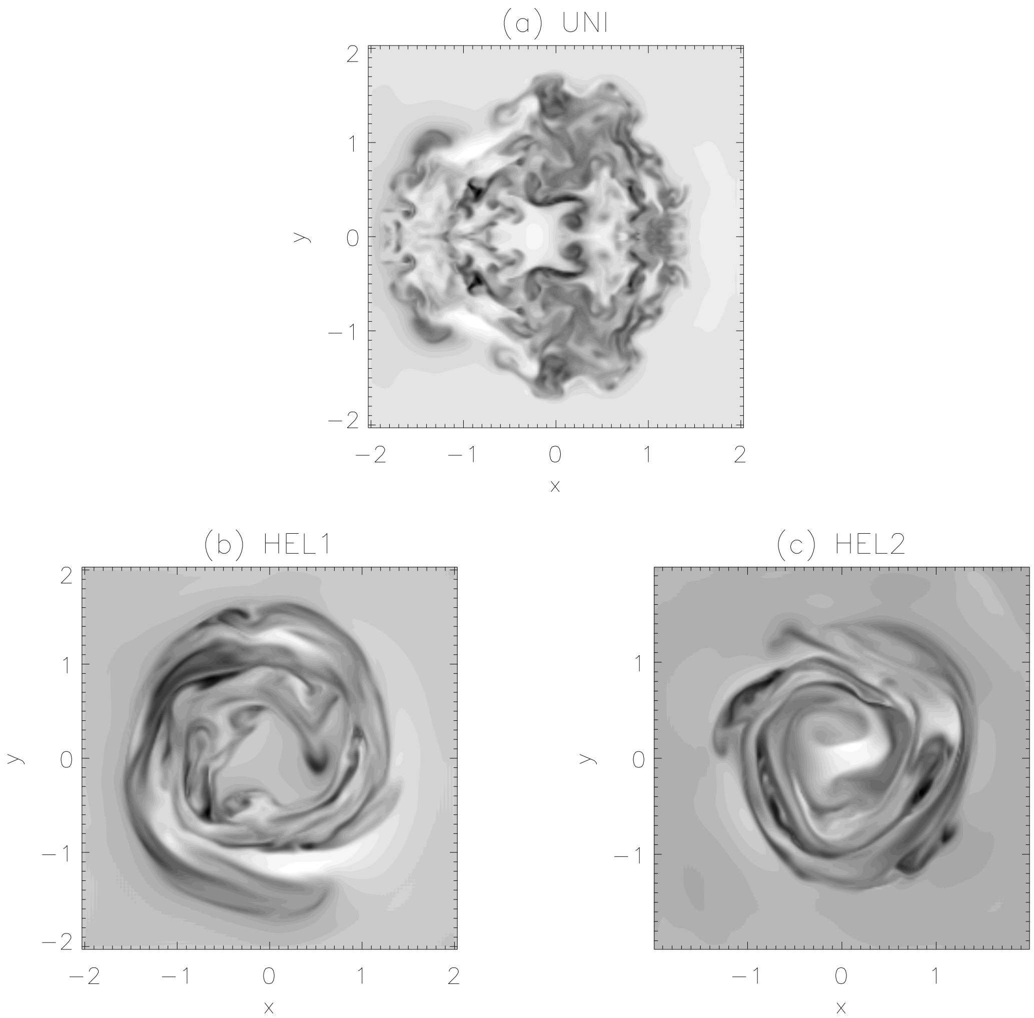

Fig. 13.— Grey scale images of the density distribution in the $x - y$ plane (using a 2D cut at $z = 1$) at the end of the simulations for time $t = 14$. Cases shown are UNI (a), HEL1 (b), and HEL2 (c). The contour levels are normalized using a linear scale with values ranging from 0.46 to 1.24.

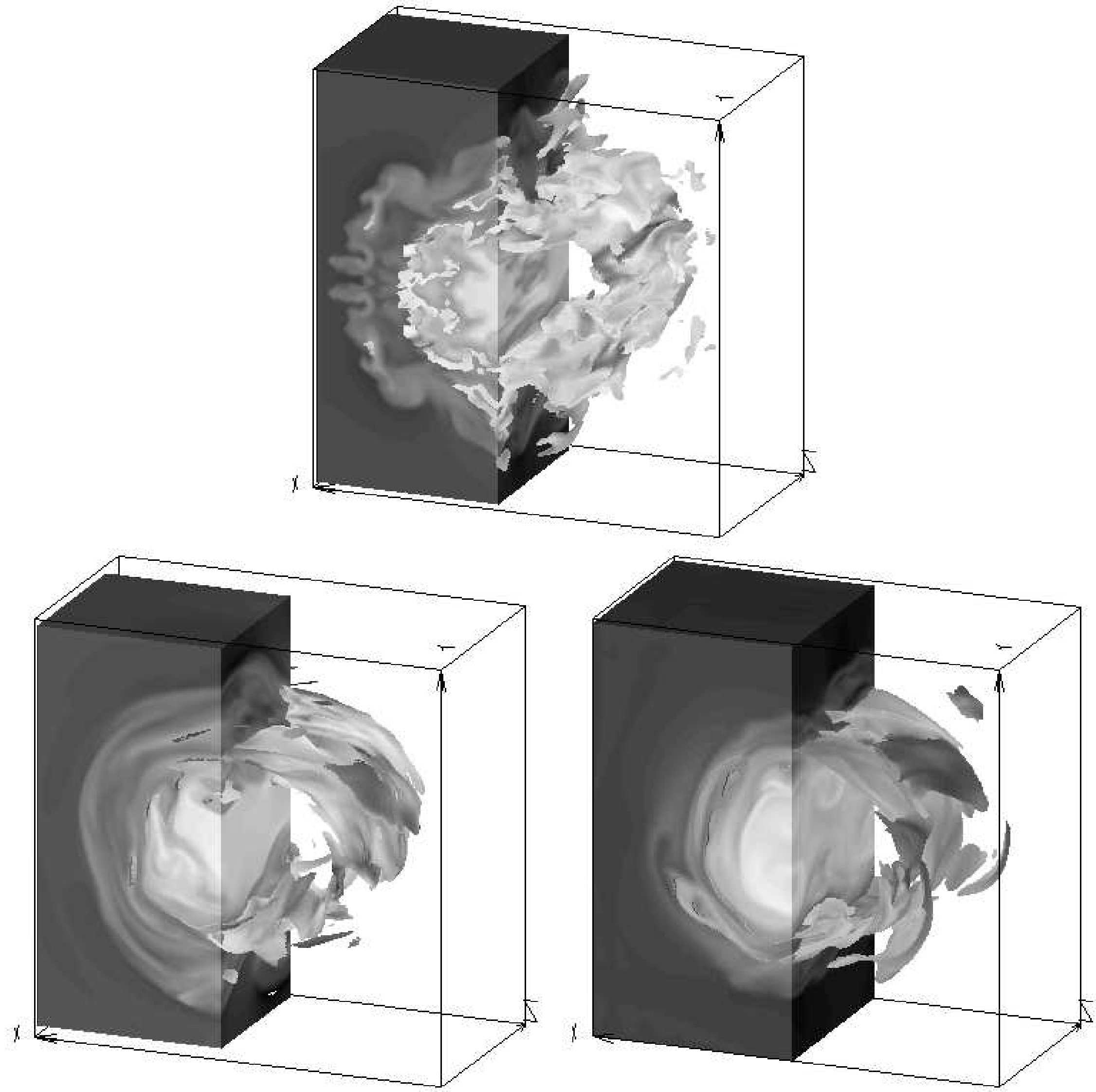

Fig. 14.— The 3D jet structure at $t = 14$ for cases UNI (top), HEL1 (bottom left), and HEL2 (bottom right). Shown is the axial velocity V_z in a grey scale on various cross-sections, as well as an isosurface $V_z = 0$ corresponding to the jet boundary.

Table 1. Initial Parameters of Simulations.

Case	r_c	$P_i(r=0)/R_j$	β_0	B_z	$B_\theta(r=R_j)$
UNI	–	∞	32	0.25	0
HEL1	2	0.5	32	0.25	0.4
HEL2	0.5	0.125	32	0.25	0.4

Note. — All simulations have been carried out with $\gamma = 5/3$, $\rho = 1$, $T_0 = 1$, $V = 1.63$, $B_0 = 0.25$, $B_1 = 1$, $R_j = 1$, $a = 0.1R_j$, and $L = 2R_j$ using a $200 \times 200 \times 100$ grid resolution. The axial sonic, fast magnetosonic, and Alfvén Mach numbers are $M_s = 1.26$, $M_f = 1.24$, and $M_{A,z} = 6.52$, respectively.